The capillary channel flow experiments on the International Space Station: experiment set-up and first results

P. J. Canfield · P. M. Bronowicki · Y. Chen · L. Kiewidt · A. Grah · J. Klatte · R. Jenson · W. Blackmore · M. M. Weislogel · M. E. Dreyer

Abstract This paper describes the experiments on flow rate limitation in open capillary channel flow that were performed on board the International Space Station in 2011. Free surfaces (gas–liquid interfaces) of open capillary channels balance the pressure difference between the flow of the liquid in the channel and the ambient gas by changing their curvature in accordance with the Young-Laplace equation. A critical flow rate of the liquid in the channel is exceeded when the curvature of the free surface is no longer able to balance the pressure difference and, consequently, the free surface collapses and gas is ingested into the liquid. This phenomenon was observed using the set-up described herein and critical flow rates are presented for steady flow over a range of channel lengths in three different cross-sectional geometries (parallel plates, groove, and wedge). All channel shapes displayed decreasing critical flow rates for increasing channel lengths. Bubble ingestion frequencies and bubble volumes are presented for gas ingestion at supercritical flow rates in the groove channel and in the wedge channel. At flow rates above the critical flow rate, bubble ingestion frequency appears to depend on the flow rate in a linear fashion, while bubble volume remains more or less constant. The performed experiments yield vast data sets on flow rate limitation in capillary channel flow in microgravity and can be utilised to validate numerical and analytical methods.

P. J. Canfield · P. M. Bronowicki · Y. Chen · L. Kiewidt ·
M. E. Dreyer (✉)
Center of Applied Space Technology and Microgravity,
University of Bremen, Bremen, Germany
e-mail: michael.dreyer@zarm.uni-bremen.de

P. J. Canfield
e-mail: peter.canfield@zarm.uni-bremen.de

A. Grah
European Commission Institute for Energy and Transport,
Petten, The Netherlands

J. Klatte
Astrium GmbH, Bremen, Germany

R. Jenson · W. Blackmore · M. M. Weislogel
Portland State University, Portland, OR, USA

1 Introduction

Open capillary channels are structures that contain a liquid with one or more free surfaces (gas–liquid interfaces) and in which capillary forces dominate the characteristics of the flow rather than gravitational forces. This can be the case in environments where gravity is reduced or compensated, e.g., in space, but also occurs on Earth when the characteristic length scale of the flow is small ($\lesssim 1$ mm). The increased importance of capillary forces in a reduced gravity environment opens the door for passive transport and control mechanisms that rely on surface tension, wettability, and geometry to perform tasks that would otherwise require bulkier and heavier equipment (Weislogel et al. 2009). For example, open capillary channels are used in propellant management devices (PMDs) of space vehicles to position and transport liquids within surface tension tanks. During acceleration phases, the liquid bulk orients itself due to body forces acting on its mass, but during non-acceleration phases the liquid may distribute itself freely within the tank. Consequentially, the outlet of the tank may lose contact with the liquid rendering the remaining propellant in the tank inaccessible for further operations unless the liquid can be transported towards the outlet again. One of the purposes of PMDs is to prevent the liquid from

becoming inaccessible. Surface tension tanks employ vanes, which are narrow and thin sheets of metal that may be positioned parallel or perpendicular to the tank's wall to form open capillary channels (Jaekle 1991). Using vanes to transport liquid from a bulk reservoir within the tank towards its outlet port is weight-efficient and also reduces the amount of moving parts, which in turn increases the device's reliability. Similar benefits can be of importance in other liquid managements systems such as those used in a space vehicle's life support systems or storage tanks. Capillary channels are also used for managing liquids in micro-electromechanical systems for lab-on-a-chip devices (Melin et al. 2005; Zhao et al. 2001), effectively reducing the need for valves and pumps in micro-scale devices that are utilised in the biological and chemical industries.

However, previous studies (Jaekle 1991; Dreyer et al. 1998; Rosendahl et al. 2004) have shown that free surfaces can collapse and cause gas ingestion in open capillary channel flows when a critical, maximum flow rate, Q_{crit}, is exceeded. This flow phenomenon is referred to as 'choking'. In certain circumstances, choking may be detrimental to the flow system. Alternatively, bubble generation may be desired in some flow systems and achieved in this way. Understanding the mechanisms of open capillary channel flow will help optimise designs that are now in use and may widen the field of viable applications. It should be noted that the capillary channel flow experiment that is presented here is an ideal case with a simplified geometry, well-defined boundary conditions, and no residual acceleration (as far as can be provided on board the ISS). The actual situation in a liquid management system on a space vehicle may differ widely in terms of residual acceleration, geometry, and boundary conditions. The aim of this paper is to provide geometrical and physical data of the set-up and to deliver results of steady flow experiments which are required for validating and improving present flow models and numerical simulations of the presented flow phenomenon. The data can also be used to benchmark state-of-the-art computational fluid dynamics software tools that solve the full Navier-Stokes equations and are commonly used in the aerospace industry.

1.1 State of the art

In reduced or compensated gravity, open capillary channel flows are subjected to changes in cross-sectional area due to pressure loss or gain in flow direction. The free surface of the open channel behaves like a flexible wall and the pressure difference Δp between the liquid in the channel p_l and the ambient pressure p_a are balanced by the local capillary pressure difference induced by the local mean curvature of the free surface in accordance with the Young-Laplace equation, $\Delta p = 2\sigma H$, where H is the local mean curvature of the interface. As the flow rate increases so does Δp, which in turn results in an increase in local curvature and a decrease in local cross section. If the flow rate is increased further, at some point the maximum mean curvature of the free surface is no longer sufficient to balance the pressure difference and gas ingestion occurs at the gas–liquid interface.

Initial analytical work on the performance of vanes as PMDs was conducted by Jaekle (1991). In this work, he demonstrated the similarity of open capillary channel flow as found in vanes to compressible flow within ducts with respect to the mechanics of flow rate limitation. The flow rate limitation in compressible flow is based on the speed of sound waves. In open capillary channel flows, the flow rate limit at which choking occurs is defined by the velocity of a longitudinal capillary wave. His proposed mathematical model predicted flow rate limitations for T-shaped vanes.

Drop tower experiments on flow rate limitation in a capillary channel composed of parallel plates were conducted by Dreyer et al. (1998) and by Rosendahl et al. (2002). Their findings substantiated the hypothesis that open capillary flows are subject to a maximum steady volume flux beyond which gas ingestion occurs due to choking. Additional experiments were performed on sounding rocket flights to increase the duration of the experiments from a few seconds to several minutes. Rosendahl et al. (2004) compared the experimental results of drop tower experiments and an experiment on-board sounding rocket TEXUS-37 with an improved one-dimensional model that incorporated both principal radii of curvature of the free surface. The numerical predictions for the profiles of the free surfaces were found to be in good agreement with experimental findings. Further experiments were conducted on sounding rockets TEXUS-41 and TEXUS-42 to determine the effect of channel length on the stability of the free surface (Rosendahl and Dreyer 2007; Rosendahl et al. 2010). It was found that increasing the channel length at a fixed flow rate could also lead to choking in the capillary channel. The extension of the one-dimensional mathematical model to incorporate accelerated flows was also compared to experiments that were performed on sounding rocket TEXUS-42 (Grah et al. 2008; Grah and Dreyer 2010).

The influence of the shape of the channel's cross section on the flow behaviour was investigated in drop tower experiments. Critical flow rates were determined for a groove-shaped channel and compared with the one-dimensional model by Haake et al. (2010). Klatte et al. (2008) used the numerical tool *Surface Evolver* (Brakke 1992) to predict three-dimensional free surface profiles and flow rate limits of steady flow in a wedge-shaped channel.

The numerical predictions were in good agreement with those of the one-dimensional model adapted for a wedge-shaped duct and with the results of drop tower experiments (Klatte 2011).

Most recently, Salim et al. (2010) performed two-phase flow experiments in an open capillary channel on sounding rocket flight TEXUS-45. Bubbly flow was generated by means of multiple needles located upstream of the test channel. Based on their observations of the free surface profile in single-phase flow and two-phase bubbly flow, they concluded that wall shear stress increases when bubbles are injected into the flow stream.

2 Materials and methods

2.1 Set-up of the experiment

The experimental hardware was manufactured by EADS Astrium and was designed to operate within the MSG on board the ISS. The interested reader will find additional information on the technical specifications of the MSG in Spivey et al. (2008). The hardware consists of four modules: two experiment units (EU1 and EU2), the electrical subsystem (ESS), and the optical diagnostic unit (ODU). EU1 and EU2 both contain the entire fluid loop in a sealed container with windows for illumination and observation of the test channel. The main difference between EU1 and EU2 is the geometry of the respective test channels, which are shown in Figs. 2 and 3. The entire fluid loop, which differs slightly between the EUs, is shown in Fig. 1. Both set-ups consists of three modules. The first set-up consists of the ESS, ODU, and EU1. A member of the ISS crew is required to install the equipment in the MSG. For the second set-up, EU1 is removed by a crew member and replaced by EU2. The ODU and ESS are compatible with both EUs and are used for both set-ups. The ESS contains the power supply and electronic control units. The ODU consists of a high-speed camera and a parallel light source. The specifications of the individual components are listed in Table 1.

In EU1, the test channel (TC) consists of parallel plates (PP) with two free surfaces opposite to each other. In EU2, the test channel consists of a wedge-shaped capillary channel (WE) with a triangular cross section, which means that it has only one available free surface. Slide bars alter the length of the channel and, in EU1, can be used to open only one side of the test channel to form a rectangular groove-shaped channel (GR) with a single free surface. The test channel is located within the test unit (TU), which provides a closed gaseous environment. Furthermore, plunger K1 is present only in EU1 and the bubble injection system (BI) is installed only in EU2.

Table 1 Specifications of the main components of the experiment hardware

Component	Dry mass (kg)	Width (mm)	Depth (mm)	Height (mm)
EU1	37.2	326	480	348
EU2	36.9	326	480	348
ESS	8.5	414	178	170
ODU	5.4	125	257	768

Experiments were performed around the clock via telemetry commanding from one of the two ground stations located in Bremen, Germany and Portland, Oregon, USA. Low rate telemetry data were recorded at both ground stations and consisted of readings from 6 pressure and 16 temperature sensors as well as from the flow meter. A low-resolution live video stream of the MSG cameras was also recorded.

2.1.1 Fluid loop

The main components of EU1 and EU2 have been tested extensively in ballistic rocket flights (Rosendahl et al. 2004; Rosendahl and Dreyer 2007) and drop tower experiments (Dreyer et al. 1998; Haake et al. 2010; Klatte 2011). The fluid loop is shown schematically in Fig. 1. Following the direction of flow, fluid passes through the test channel (TC), valve C4, the pump (P), the flow meter (F), the phase separation chamber (PSC), the flow preparation chamber (FPC), valve C9 and then re-enters the test channel. The length of the test channel is the length of the free surface which is defined by the distance between the pinning edges of the inlet and outlet of the test channel. The pinning edge at the inlet of the test channel is stationary and points downstream. The pinning edge at the outlet of the test channel is located on the end of the sliders that points upstream. The thickness of each pinning edge is 0.2 mm. The sliders (S1, S2) can be moved individually to vary the length of the test channel within the range $0.1 \text{ mm} \leq l \leq 48 \text{ mm}$. The slider actuators are piezo linear motors that allow a high degree of accuracy (± 0.05 mm). Flow is considered to be laminar throughout the experiments as Reynolds numbers[1] are consistently lower than 1,800 at the inlet of the channel.

The test channels are made of quartz glass. In EU1, the test channel consists of parallel plates (see Fig. 2). The distance between the glass plates is $a = 5$ mm, and the height of the channel is $b = 25$ mm. In EU2, the test channel has a triangular cross section with an opening

---

[1] $Re = \bar{u}_0 D_h v^{-1}$, where $\bar{u}_0$ is the mean velocity at the inlet of the TC and v is the kinematic viscosity of the liquid. D_h is the hydraulic diameter with $D_h = 4A_0/P$ and P is the wetted perimeter.
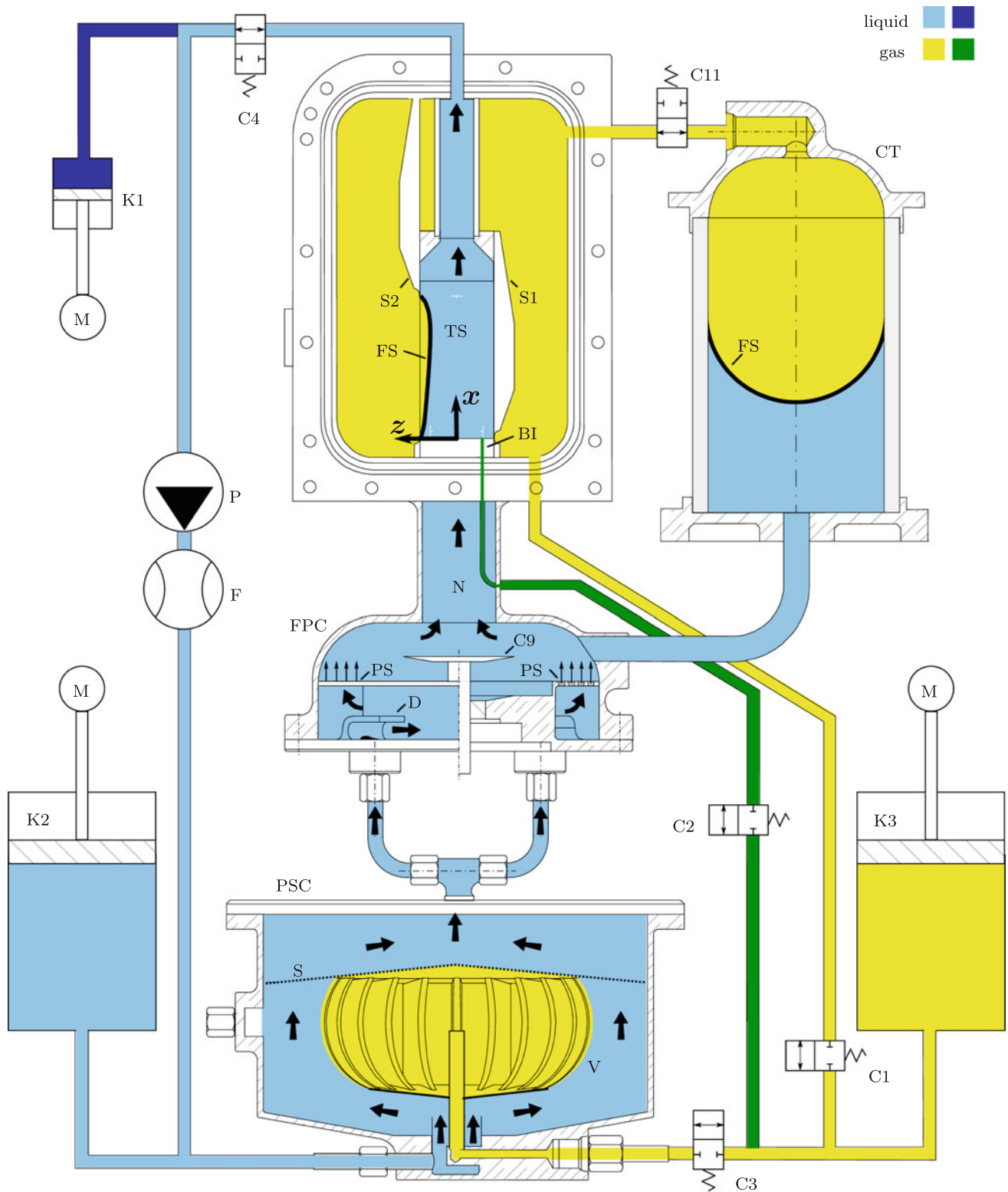
Fig. 1 Schematic of the fluid loop inside each EU. The fluid management system contains liquid (*cyan* and *ultramarine*) and gas (*yellow* and *green*). Ultramarine lines exist only in EU1 and *green lines* exist only in EU2. The main components of the fluid loop are the test channel (TC) with a free surface (FS), the pump (P), the phase separation chamber (PSC), the flow preparation chamber (FPC), and the compensation tube (CT). The TC shown here is only valid for EU1, because in EU2 only one slider (S1) is present
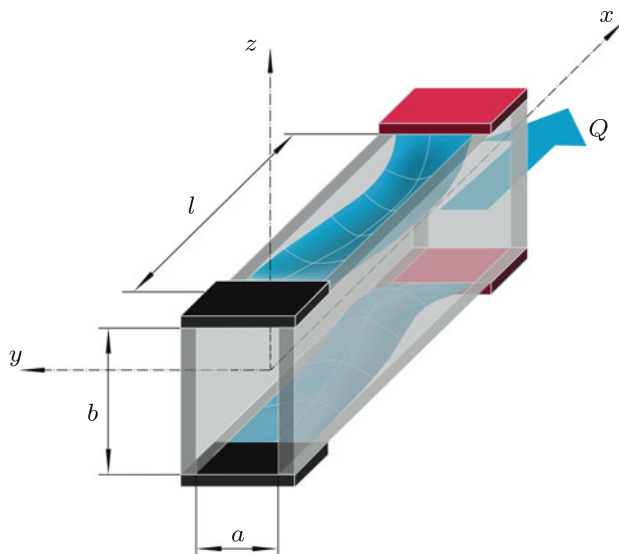
Fig. 2 Liquid flowing through parallel plates that form an open capillary channel. The geometry of the channel is defined by its length l, its width a, and its height b

Fig. 3 Liquid flowing through a wedge that forms an open capillary channel. The geometry of the channel is defined by its length l, its opening angle 2α, and its height b. A gas injection needle is located above the vertex at the inlet of the channel

angle of $2\alpha = 15.8°$ (see Fig. 3). The height of the test channel is $b = 30$ mm and the distance between the tilted faces at the top of the channel is $a = 8.32$ mm. The cross-sectional area of the inlet of both test channels is $A_0 = 125$ mm^2.

The geometry of the fluid loop in the vicinity of the test channel of EU1 is shown in Figs. 1 and 4. The total cross-sectional area of the FPC is 7,238 mm^2, but the flow passes along deflectors (D) and through a perforated sheet (PS) to enter the FPC with an assumed uniform velocity distribution. The sum of the perforations in the PS reduces the effective inlet area to $A_{FPC} = 1,018$ mm^2 through which flow is possible. Upstream of the test channel, the nozzle is $s_1 = 30$ mm long and has an elliptical contour in the xy-plane in EU1 and in both planes in EU2. The cross-sectional area of the nozzle's inlet is $A_{N1} = 750$ mm^2 and $A_{N2} = 609$ mm^2 for EU1 and EU2, respectively. At its outlet, the cross section of the nozzle is identical to A_0. The nozzle is connected to the test channel by a closed entrance duct with a cross section that is identical to A_0. The length of the entrance duct is $s_2 = 33.3$ mm. As explained above, the length of the test channel is variable with $s_3 = l$. Downstream of the test channel, liquid passes through an exit duct which has the same cross section as the test channel. The length of the exit duct depends on the length of the test channel such that $s_4 = 67$ mm $- l$. The cross section then constricts over a length of $s_5 = 12.8$ mm to a circular cross section with a diameter of 10.7 mm.

The compensation tube (CT, Fig. 1) is cylindrical and has a diameter of 60 mm and a height of 100 mm. Its cylindrical wall is transparent so that the fill level m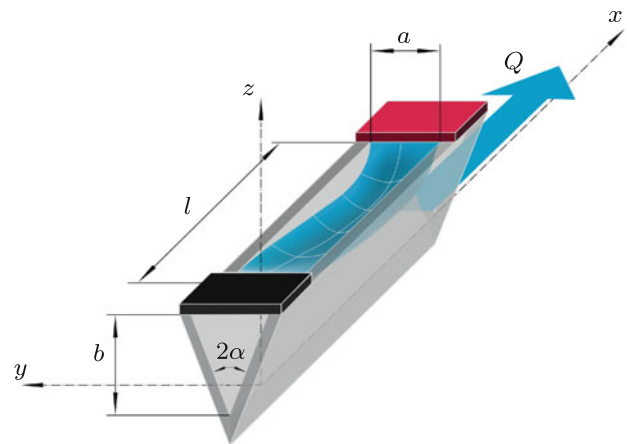ay be observed during operations. The compensation tube provides an additional free surface (FS) in the system. This liquid meniscus defines the static pressure at the inlet of the test channel. The compensation tube also compensates varying volumes during unsteady flow. For example, when gas is ingested or injected into the liquid loop, liquid is displaced and the fill level in the compensation tube rises without changing the pressure boundary conditions of the test channel. The liquid in the compensation tube is connected to the liquid in the flow preparation chamber by a tube that is 97.7 mm long with an inner diameter of 7.75 mm and bends by 90°. The gas in the compensation tube is connected to the gas environment in the TU. This connection may be closed using valve C11.

The forced flow is maintained by a Micropump GB-P25 pump head and a Maxon EC32 brushless motor. In the experiments, the flow rate Q is limited to a maximum flow rate of $Q \leq 20$ cm^3 s^{-1}. Both flow rate and flow acceleration can be varied in the experiments. The flow meter is a DPM-1520-G2 turbine flow meter from Kobold and is calibrated to an accuracy of ± 0.1 cm^3 s^{-1}.

K2 and K3 are plunger bellows and are the reservoirs for the liquid and the gas phases, respectively. Both bellows have an operational volume of 273 cm^3. Between experiments, the plungers are used for fluid management and setting boundary conditions including the fill level within the CT, the gas volume within the PSC, and the pressure within the gaseous environment surrounding the test channel. When choking occurs, these parameters change during the experiment because the ingested gas is collected in the PSC and displaces volume in the CT. Plunger K1 can impose an oscillation on the flow rate at the outlet of the test channels in EU1 with volume amplitudes of up to ± 0.5 cm^3 and frequencies up to 10 s^{-1}. Experiments with oscillatory excitation of the flow rate were conducted
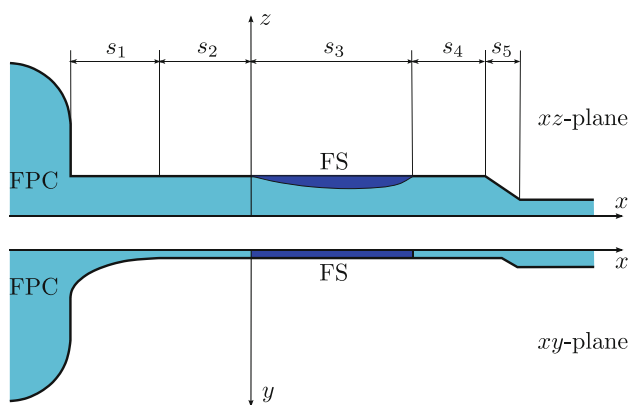
Fig. 4 Geometry of the fluid loop in the vicinity of the test channel of EU1. The test liquid is *coloured cyan*, *dark blue* represents the gas–liquid interface. The geometry in the xz-plane is shown on top, and the geometry in the xy-plane is shown below. Both views are cut in the respective symmetry planes. Flow direction is from *left* to *right*. Starting from the flow preparation chamber (FPC), liquid flows through the nozzle (s_1), entrance duct (s_2), test channel (s_3) with the free surface (FS), and exit duct(s_4). Downstream of the test channel, the duct changes along s_5 to a circular cross section

Fig. 5 Sketch demonstrating the bubble sensor system in the PSC. During the experiments, the interface of the bubble in the PSC was always located somewhere between sensor 1 (*yellow bubble*) and sensor 3 (*green bubble*). The test liquid is *coloured blue* and the vanes (V) keeping the bubble in the centre are *grey*

over the entire frequency range with flow rate variations in the range of ±0.01 to ±0.5 cm^3 s^{-1}.

In EU2, a bubble injection system is integrated into the fluid loop. A needle penetrates the wall of the entrance duct opposite the vertex of the channel and is bent around to finally point in flow direction. The outlet of the needle is located at the inlet of the test channel ($x = 0$) approximately 3.6 mm above the vertex of the wedge (see Fig. 3). The needle has an inner diameter of 0.6 mm and an outer diameter of 0.8 mm. Gas injection frequency and bubble size can be altered by defining the operating parameters of C2 which is a solenoid valve of model MHE2-MS1H-3/2O-M7 from Festo. The frequency of valve C2 can be set from 0 Hz (valve closed) to 10 Hz (gas line open once per 0.1 s). The duty cycle of valve C2 defines how long the gas line is open and can be set to values between 0 and 10 s.

The PSC is designed to gather any gaseous phase which may have entered the fluid loop and prevent it from re-entering the test channel. Gas is trapped in the PSC by a porous screen (S, Fig. 1) that has a nominal pore size of 5 m. A bubble-shaped vane structure (V, Fig. 1) ensures that gas is kept in the centre of the PSC. The size of the bubble in the phase separation chamber is determined qualitatively using three 10K3MCD1 Betatherm NTC thermistors which have an accuracy of ±0.2 °C at 25 °C. Dissipation of the heat that is generated by the thermistors depends on the properties of the fluid that it is immersed in. In this way, local temperature measurements indicate the presence of the gaseous or liquid phase. The three thermistors are located along an axis as indicated in Fig. 5. Based on *Surface Evolver* (Brakke 1992) computations, the bubble
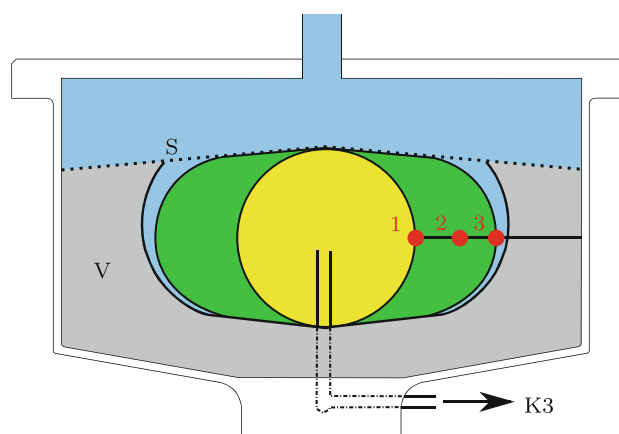
volume at bubble sensors 1, 2, and 3 is estimated to be 90, 150, and 200 cm^3, respectively. During the experiments, the interface of the gas bubble in the PSC was located between bubble sensor 1 and bubble sensor 3. Gas can be extracted from the PSC through a needle that protrudes into its centre (see Fig. 1). The needle is connected to plunger K3 via valve C3. As already discussed, re-entry of the liquid flow into the test channel occurs after passing through the FPC where a uniform laminar flow is developed by means of deflector plates, a perforated sheet, and the nozzle.

The test fluid that was used in the experiments is the commercially available 3M^{TM} Novec^{TM} 7500 Engineered Fluid, which is a hydrofluoroether that is generally used for heat transfer and for cleaning electronics. The properties of the test liquid are listed in Table 2 for the temperature range that is relevant for the experiments. The amount of test liquid in the system is 1.68×10^3 cm^3. The gaseous environment consists of nitrogen. During operations, the system pressure was typically in the range of 0.95×10^5 Pa to 1.15×10^5 Pa.

The temperature within the experimental set-up is monitored at various locations within the liquid and gas loops using PT1000 resistance temperature detectors from Honeywell with an accuracy of ±0.5 °C within the temperature range that was used in the experiments. The pressure is monitored in the gas duct near plunger K3, in the FPC, and in the gas environment surrounding the test channel. The pressure sensors are PAA-33X models from Keller, which are calibrated to an absolute accuracy of less than 10^2 Pa. Throughout the experiments, the temperature remained within the range of 25–35 °C. The average temperature in EU1 operations was 30.4 °C, and in EU2, it was 29.8 °C. Cooling of the experiment apparatus is

Table 2 Density ρ, viscosity ν, and surface tension σ of the test liquid Novec^{TM} Engineered Fluid HFE-7500 at different temperatures T. Its static contact angle on quartz glass is $\gamma = 0°$

T (°C)	ρ (kg m^{-3})	ν ($\times 10^{-6}$ m^2 s^{-1})	σ ($\times 10^{-3}$ kg s^{-2})
25.0	$1{,}620 \pm 2$	0.773 ± 0.1	16.66 ± 0.1
30.0	$1{,}610 \pm 2$	0.715 ± 0.1	16.16 ± 0.1
35.0	$1{,}600 \pm 2$	0.664 ± 0.1	15.67 ± 0.1

performed by the MSG work volume air circulation system and air handling unit, which provide 200 W of cooling power (Spivey et al. 2008). In addition, each EU is equipped with a thermal control system (TCS) with thermoelectric coolers, which transfer heat between the liquid loop and the air in the MSG work volume.

2.1.2 Optical set-up

The ODU consists of a high-speed high-resolution camera (HSHRC) and a parallel light source that are positioned perpendicularly to the outer walls of the test channel (see Fig. 6) thus recording in the xz-plane of the respective test channels (compare Figs. 2, 3). The camera is a Motion BLITZ Cube 26H from Mikrotron, which can record up to 250 frames per second at a resolution of $1{,}280 \times 1{,}024$ pixels per frame. A large-field telecentric lens is attached to the camera. The test channel is illuminated by a Correctal TC parallel light source from Sill Optics. The LEDs emit light at a wavelength of 455 nm, which corresponds to the wavelength sensitivity of the CCD chip in the camera. The parallel light source and the HSHRC are mounted on an optical bench to ensure they are aligned along an axis. The HSHRC is set up to capture the entire test channel. The optical resolution of the test sections is computed to be 0.038 mm/pixel. The field of view contains the test channel and covers an area of 49.3 by 39.4 mm. Recorded data are processed on board and then transferred to the MSG Laptop Computer (MLC) and subsequently to the ground stations. The on-board image processing software contains an edge detection algorithm and converts the recorded 8-bit monochrome images to binary images. On-board image processing reduces the file size considerably and increases download efficiency.

Further image analysis is performed later to evaluate the contour of the free surface in the test channel based on the processed black and white images. The combination of on-board image processing and subsequent analysis of the contour leads to an error of approximately 2–3 pixels, which corresponds to less than 0.12 mm.

Additional Hitachi HV-C20 CCD cameras that belong to the inventory of the MSG were installed to observe the CT (MSG camera 1) and the test channel (MSG camera 2).
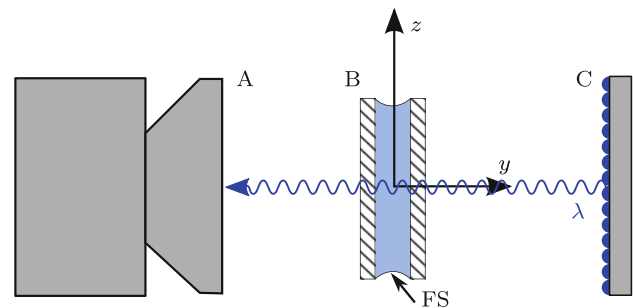

Fig. 6 Optical set-up for the HSHRC (not to scale) with the camera (A), the test channel (B), and the light source (C). Light that is refracted at the free surfaces (FS) appears in recorded images as a *black area* with a well-defined edge against the illuminated background

Throughout operations one ISS video channel was dedicated to broadcasting a live stream of one of the MSG cameras. The images of one of the cameras were broadcast as a live stream to the ground stations at a frame rate of at least 8 fps. Throughout all experiments, video data were recorded from the live stream obtained from one of the MSG video cameras.

2.1.3 Electrical subsystem

The ESS contains all required electronic boards including the motion controllers and the CCF computer. The CCF computer is a MOPS-PM from KONTRON with 512 MB RAM and a 1 GHz Intel Celeron M processor. Two 512 MB compact flash memory cards are used as hard drives. The ESS connects to the MSG for power supply and for data transfer. Furthermore, an ethernet connection is established to the MSG laptop computer and is dedicated to downloading science data from the CCF computer. One of the main tasks of the CCF computer is to convert the grey-scale images recorded by the HSHR camera into black and white images to reduce the data volume. At all times, the ESS requires less than 200 W to power the entire experiment set-up. Therefore, the total power consumption at any given time is less than the heat exchange capability of the MSG work volume air handling unit mentioned in Sect. 2.1.1

2.2 Initial filling procedure

During transportation and installation of the EU, all valves in the fluid loop are closed, the CT and PSC are completely filled with the test liquid, and the line between C9 and C4 contains only gas. Before nominal operations can commence, the following procedures must be performed:

– a gas–liquid interface must be established in the CT,
– a bubble must be injected into the PSC,
– the test channel must be filled with the test liquid.

Generating a gas–liquid interface in the CT must be accomplished first so that liquid that is displaced by injecting gas into the PSC can be compensated. This is accomplished by opening valve C11 and then pulling liquid into reservoir K2. Care must be taken to prevent liquid from exiting the CT through C11 when it is opened. This can be prevented by setting the pressure of the gas in the TU slightly higher than that of the liquid in the CT by opening C1 and altering the gas volume in reservoir K3. Approximately 75 % of the liquid in the CT is transferred to the previously almost empty reservoir K2.

Next, a bubble is introduced into the PSC. As mentioned above, gas can be transferred from the gas reservoir K3 to the PSC and vice versa. The needle that protrudes into the centre of the PSC is connected to K3 via valve C3 (see Fig. 1). A sufficiently large bubble is required to ensure that the needle is located well within the bubble. Later, when gas has been ingested into the liquid loop due to choking, it can be retrieved from the PSC without also extracting liquid and subsequently relocated into the test unit, thereby restoring the ambient pressure boundary condition. Before opening valve C3, care must be taken that the pressure in the gas reservoir is higher than that of the liquid in the PSC thus avoiding flow of liquid into the gas lines. Then, gas is introduced stepwise into the PSC until the bubble interface has reached bubble sensor 1 and its size is approximately equal to that of the yellow region in Fig. 5. At this moment, all valves are closed and the procedure for filling the TC can be performed.

The procedure for filling the TC differs between EU1 and EU2. In EU1, the TC is filled from both sides sequentially. With the slider opened to 34.4 mm valve, C4 and C11 are opened and then liquid is transferred from K2 through C4 into the TC until the advancing meniscus is observed at the outlet of the TC. Then, C4 and C11 are closed again. Once all valves are closed, C9 is opened and liquid is transferred from K2 through the inlet of the TC until the meniscus at the outlet coalesces with the interface advancing from the inlet. Then, C11 is opened again and a low flow rate is established with the pump

In EU2, the TC is filled only from the outlet. First, the slider is moved to open the TC by 20 mm. Then, valve C4 is opened and liquid is transferred from K2 into the TC. The amount of liquid in the TC is increased in small steps and corner flow at the vertex of the wedge transports a portion of the liquid towards the inlet of the TC and C9. This is continued until the TC is filled from both sides and the gas in the TC has been expelled completely. Then, valves C9 and C11 are opened and a low flow rate is established by the pump.

Once the filling procedure is completed, nominal operations commence and science data can be gathered. For each EU, the entire initial filling procedure was completed within 8 h. The filling procedure is performed via telecommanding from the ground stations

2.3 Procedure of experiment

In the steady flow experiments, the critical flow rate, Q_{crit}, is defined as the maximum flow rate at which a stable free surface is observed. Once Q_{crit} is exceeded, the free surface collapses and bubbles are ingested into the channel. Q_{crit} was determined by a step-wise approach in the experiments. Beginning at a flow rate at which the free surface was stable, the flow rate was increased by 0.05 cm^3 s^{-1} (EU1) or 0.01 cm^3 s^{-1} (EU2) over a time interval of 1 s. Once the new flow rate was reached, the free surface was observed for a time period of at least 30 s to determine its stability. These experiments were performed for all three geometries. The channel length was varied between experiments and critical flow rates were determined within the range of 1 mm $\leq l \leq$ 48 mm. High-speed camera footage was recorded for each of the presented critical flow rates. The duration of the recordings could be varied and was typically selected to between 2 and 20 s depending on the selected frame rate. Once the recording had finished, on-board image processing was initiated, which typically took approximately 30 min to complete. The result files were then downloaded to a file server by NASA's MSG ground control and could finally be accessed by the research teams.

3 Results and discussion

3.1 General performance of experiment

Hardware installation on board the ISS took place on December 27, 2010, for EU1 and operations lasted until March 17, 2011. Installation of EU2 was completed on September 19, 2011, and operations lasted until October 17, 2011. Installation on board the ISS was performed excellently by Commanders Scott Kelly and Mike Fossom for EU1 and EU2, respectively. The installation procedure required less than 3 h of crew time for each EU. After installing the hardware, no further crew involvement was required for nominal operations until the end of operations, when the experiment was removed from the MSG and placed in stowage by astronauts Catherine Coleman and Mike Fossom for EU1 and EU2, respectively. Prior to removal from the MSG, the set-up was returned to its pre-installation status as well as possible. This involved removing gas from the PSC, filling the CT with liquid, and

closing all valves. The test channel was not drained for stowage.

The experiment hardware was controlled from two ground stations, one located at ZARM in Bremen, Germany, and the other at Portland State University in Portland, Oregon, USA. This enabled the research team to gather data around the clock with the research teams on either side of the Atlantic taking turns to command the experiment. The data connection to the experiment was reasonably direct with only a few seconds passing from initiating a command from the ground station and observing the response in the telemetry data and the video feed. Over 4,000 individual experiments were performed and documented over the course of approximately 2,400 h of experimental operations. The steady flow experiments account for approximately a fifth of the total number of data points gathered. The experiment hardware, especially the fluid loop, proved resilient against oscillations and accelerations that were caused by manoeuvres of the ISS, but no science data was collected when such disturbances of microgravity occurred. The combination of pump, sensors, plungers, and valves was also used to maintain the fluid loop when necessary. They were also used to adjust the system pressure, the fill level in the CT, and the size of the bubble in the PSC.

Commanding of the experiment hardware and reception of its telemetry data were limited to periods of acquisition of signal (AOS), when a data connection to the ISS was available. During loss of signal (LOS), no data was received and the ability to command the experiment was suspended by NASA ground control. Therefore, no experiments took place during these periods. Prior to scheduled LOS phases, the experiment was set to a 'safe' mode, in which the test channel is closed and a low flow rate is established. The duration of AOS periods was typically around 1 or 2 h with short LOS intervals of less than an hour between them, but these durations differed based on current operations on the ISS and satellite coverage. Furthermore, experiments were suspended when docking or reboost procedures were performed on board the ISS.

3.2 Critical flow rates

Critical flow rates were determined for steady flow conditions in the range of 1 mm $\leq l \leq$ 48 mm and the results are presented in Fig. 7. The error is determined by the accuracy of the flow meter. At various channel lengths, Q_{crit} was determined multiple times to ensure repeatability of the results. The standard deviation between the observed Q_{crit} for a given channel length was lower than the accuracy of the flow meter. All three geometries display decreasing values for Q_{crit} with increasing l. For short channels with $l < 20$ mm, the decline of Q_{crit} appears
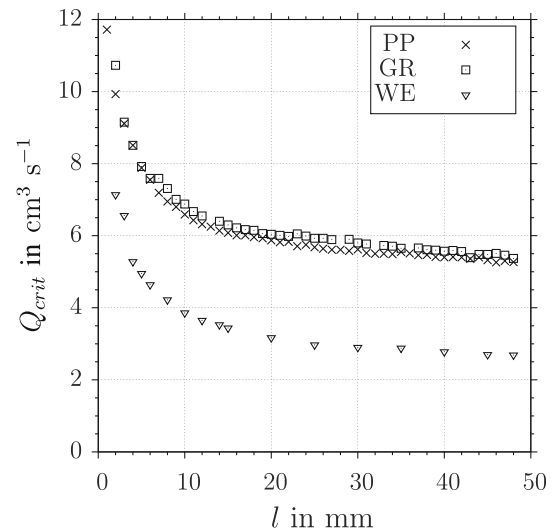

Fig. 7 Experimentally determined critical flow rates for steady flow for the individual test channel shapes: parallel plates (PP), groove (GR), and wedge (WE)

hyperbolic. For longer channels with $l \geq 20$ mm, the decline of Q_{crit} appears to be linear. As discussed in Rosendahl et al. (2004), this could be explained by the transition from an inertia dominated flow regime towards a viscous dominated flow regime as the flow rate decreases. The difference between the geometries is most significant in the wedge. The values of Q_{crit} are significantly lower in the wedge-shaped channel than in the parallel plates or groove channels, which, in comparison, hardly differ from each other (on average a difference of 3 %). The highest critical flow rates attained at a given channel length within the observed range are found in the groove geometry.

3.3 Behaviour of the free surface

The behaviour of the free surface in the experiments at steady flow rates can be divided into two categories, stable and choked. Examples of both categories are given for each channel geometry in Figs. 8, 9, 10, 11, 12, 13. The free surface is visible as a black area on the open sides of each channel. The height of the free surface, k, is an indication of the pressure difference between the flowing liquid in the test channel and the ambient gas. In Figs. 8, 10, and 12, the flow rate has not exceeded Q_{crit}. Minor oscillations can be observed on the free surface which are believed to emanate from vibrations caused by the gear pump that generates the flow. Besides these oscillations, the free surface is stable throughout the entire duration of the experiment in each of the geometries. In Figs. 12 and 13, the length of the channel has a more pronounced effect on the slope of the free surface than in Figs. 10 and 11, where the channel is longer.
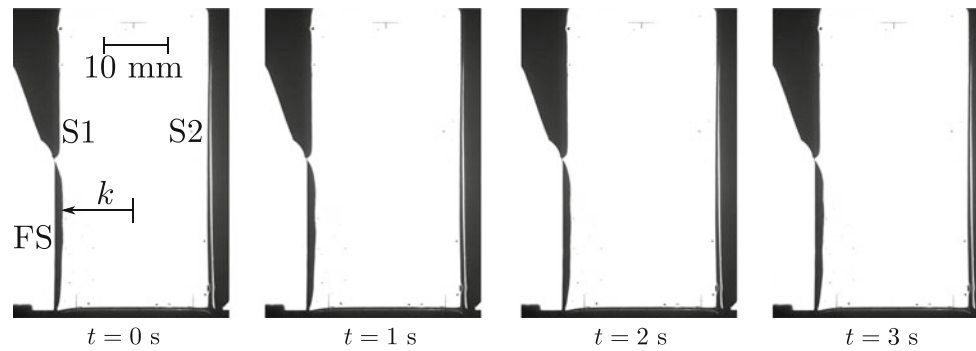
Fig. 8 Selected unprocessed images from experiment GR174 showing stable flow from *bottom* to *top* in the groove channel at $Q = 5.24 \pm 0.1$ cm^3 s^{-1} with $l = 25$ mm. One of the sliders (S1) is open and the other (S2) is closed. The free surface (FS) is visible as a *black area* bending into the *left* side of the channel. The position of the free surface within the channel is indicated as k. Additional shadows at the inlet of the channel and in the vicinity of the sliders (S1 and S2) are a result of liquid menisci on the outer surface of the glass plate
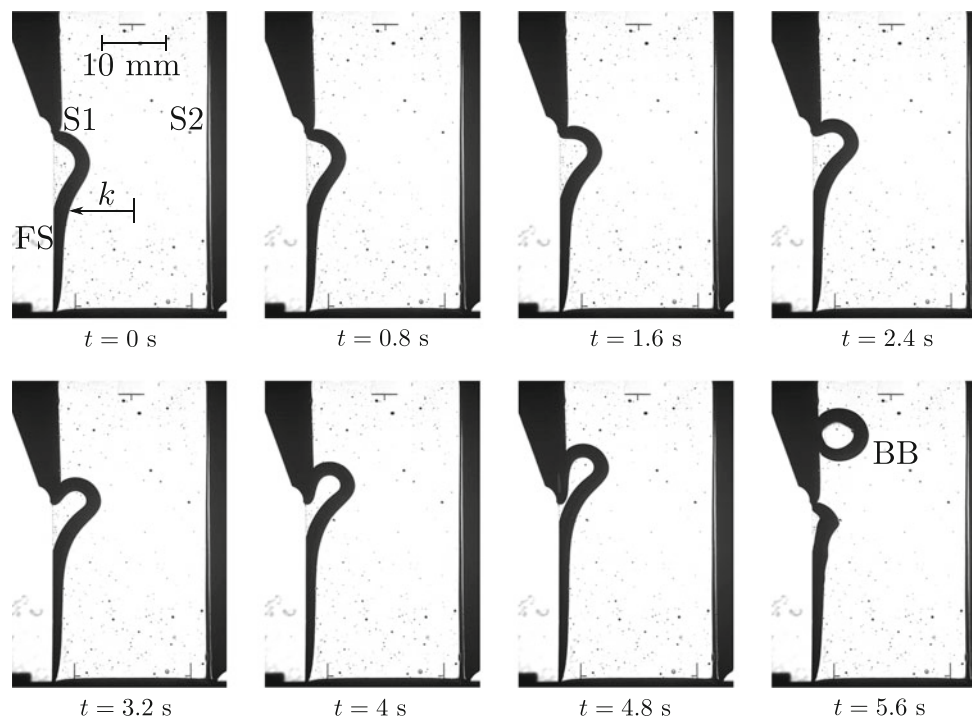
Fig. 9 Selected images from experiment GR59 showing choked flow from *bottom* to *top* in the groove at $Q = 5.95 \pm 0.1$ cm^3 s^{-1} with $l = 29$ mm. The position of the free surface within the channel is indicated as k. During the experiment, the free surface (FS) proceeds to bend further into the channel until gas is ingested. Once the bubble (BB) is detached, the free surface retracts almost completely and the ingestion process starts over

In Figs. 9, 11, and 13, examples are given for choked flow in each of the geometries. In each of the experiments, the flow rate has exceeded Q_{crit}. In these cases, the maximum mean curvature of the free surface is no longer sufficient to balance the pressure difference between the liquid in the channel and the ambient gas pressure. The free surface continues to bend further into the channel until a gas bubble is ingested into the liquid. Immediately after gas ingestion, the free surface snaps back and the process repeats itself. In the groove and wedge-shaped channels,

ingestion is only possible on one side because only one free surface is present. However, in the parallel plate channel, gas ingestion is possible on both sides. As can be seen in Fig. 11, both free surfaces proceed to bend further into the channel almost identically once Q_{crit} is exceeded. However, at some point, one free surface is favoured over the other and the opposite free surface retracts slightly before a bubble is ingested into the liquid. After bubble ingestion, the process repeats itself until the flow rate is reduced sufficiently.
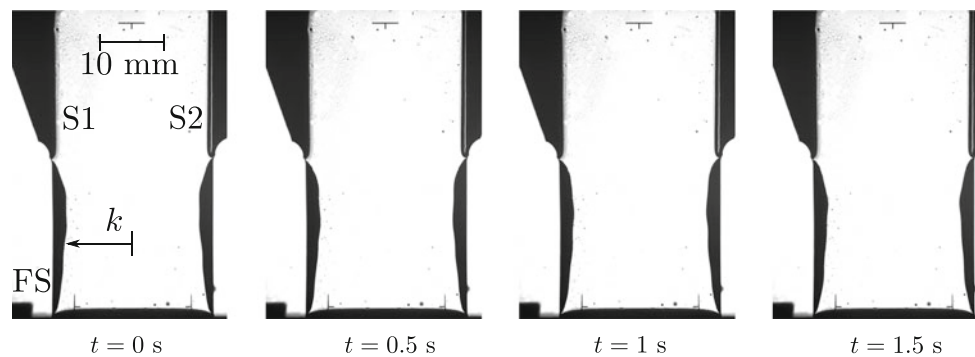
Fig. 10 Selected images from experiment PP740 showing stable flow from *bottom* to *top* in the parallel plate channel at $Q = 5.73 \pm 0.1$ cm^3 s^{-1} with $l = 25$ mm. Both sliders (S1 and S2) are open. The stable free surfaces are visible as the *black areas* bending into either side of the channel
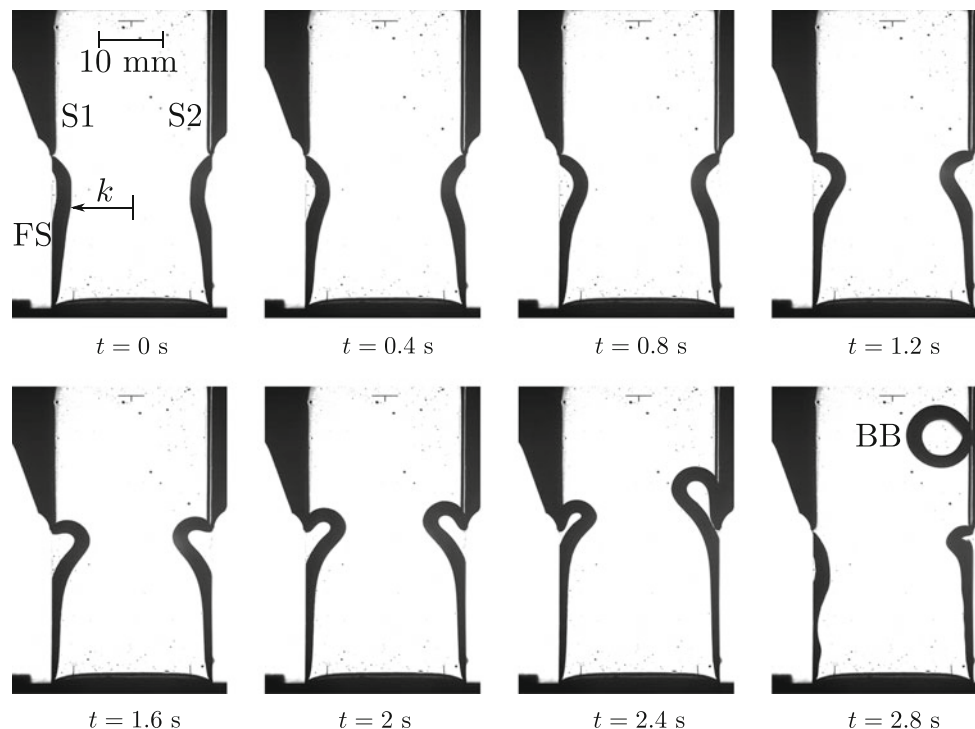

Fig. 11 Selected images from experiment PP715 showing choked flow from bottom to top in the parallel plate channel at $Q = 5.72 \pm 0.1$ cm^3 s^{-1} with $l = 25$ mm. During the experiment, both of the free surfaces (FS) proceed to bend farther into the channel. At the beginning of the instability, both surfaces bend symmetrically. Prior to gas ingestion, one of the free surfaces retracts slightly and the other collapses. As soon as gas is ingested on one side of the channel (here on the *right*), both free surfaces retract almost completely

Images recorded by the HSHR camera display artefacts that appear as specks on the test channel and can be seen in Figs. 9 and 13. The source of these specks is unknown, and they were observed before the initial filling procedure. The visibility of the artefacts depended on the lighting conditions, and although the degradation of the image quality is a nuisance, the flow within the test channel was not affected. The number of specks and their location was impervious to flow conditions within the TC. These observations lead the authors to the conclusion that the source of the specks is located outside the test channel and can therefore be neglected.

3.4 Bubble ingestion behaviour

Choking and bubble ingestion occurs in steady flow when the critical flow rate Q_{crit} is exceeded. Experiments were performed at supercritical flow rates $Q = Q_{crit} + \Delta Q$
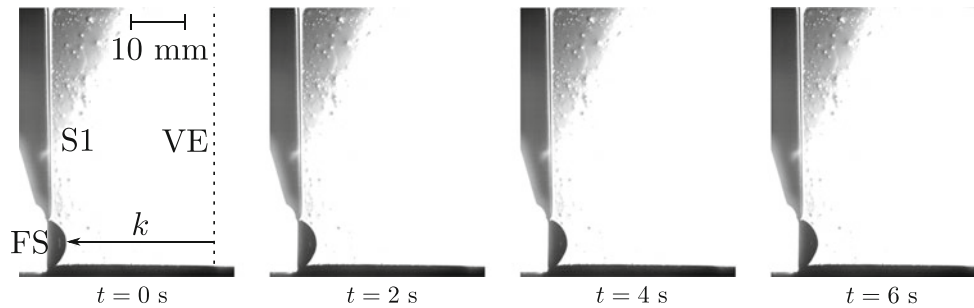
Fig. 12 Selected images from experiment WE1125 showing stable flow from bottom to top in the wedge-shaped channel at $Q = 3.87 \pm 0.1$ cm^3 s^{-1} with $l = 10$ mm. The vertex (VE) of the wedge is indicated by the *dashed line*. The position of the free surface within the channel is indicated as k. The stable free surface is visible as the *black area* bending into the channel at the lower left side of the image
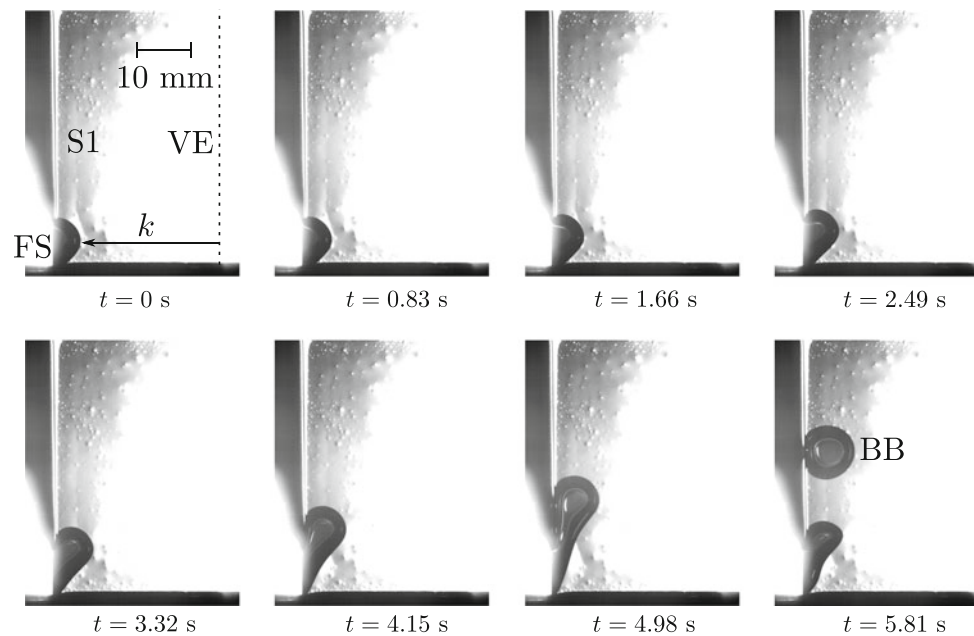

Fig. 13 Selected images from experiment WE1433 showing choked flow from bottom to top in the wedge-shaped channel at $Q = 3.93 \pm 0.1$ cm^3 s^{-1} with $l = 10$ mm. The vertex(VE) of the wedge is indicated by the *dashed line*. During the experiment, the free surface proceeds to bend further into the channel. As soon as gas is ingested as a bubble (BB), the free surface begins to retract

without the use of the bubble injector to determine whether the gas ingestion behaviour changes when the flow rate is increased further. The flow rate difference $\Delta Q = Q - Q_{crit}$ is positive for supercritical flow. Bubble ingestion frequencies f_{ch} and bubble volumes V_{BB} were determined for selected channel lengths and only in the groove and wedge channels. Multiple ingestion events were recorded for each data point and the presented results of f_{ch} and V_{BB} are averaged values.

The mean diameter $\bar{D}_b$ of all ingested bubbles for each V_{BB} was measured in the xz-plane (compare Figs. 2, 3). Non-circularity of bubbles in the xz-plane is accounted for by determining a mean diameter for each

individual bubble by measuring D_b at multiple angles β. All ingested bubble diameters were found to be larger than the channel's width, which means that they cannot be spherical but are confined between the plates and have a shape that resembles a cheese wheel. As the test liquid is perfectly wetting, the outer rim of the bubbles is curved and tangential to the test channel's walls. As the recorded images only show the xz-plane, the three-dimensional shape of the bubbles can only be assumed. The shape of the bubble that is used to calculate V_{BB} is shown on the left hand side of Fig. 14. The volume of the bubble in EU1 can then be calculated as the sum of the outer half of a ring torus and an inner circular
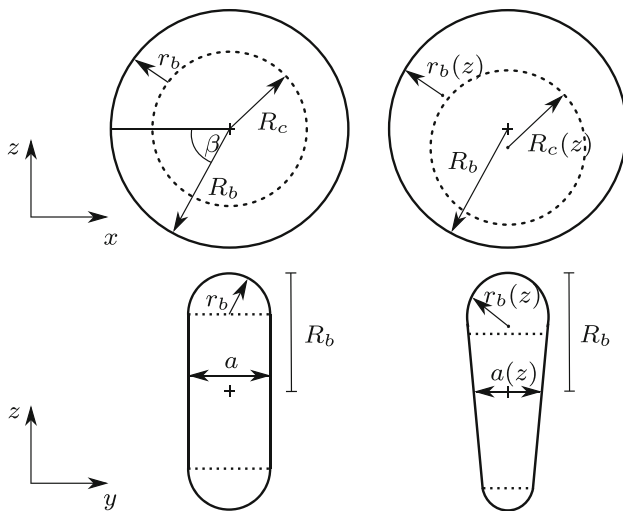
Fig. 14 Assumed shape of the ingested bubbles in the *xz*-plane (*top*) and the *yz*-plane (*bottom*). In EU1, the channel's walls are parallel, and thus, the bubble has parallel interfaces (*left*). The tilt of the walls of the wedge in EU2 is taken into consideration for the assumed shape of the ingested bubbles (*right*)

cylinder as indicated in Fig. 14 with the total volume V_{BB} given as

$$V_{BB} = \pi^2 r_b^3 \left(\frac{R_b}{r_b} + \frac{4}{3\pi} - 1 \right) + 2\pi r_b (R_b - r_b)^2 \quad (1)$$

where $R_b = 0.5 D_b$ is the measured radius of the bubble and r_b is assumed to be equal to $0.5a$.

In EU2, the ingested bubbles are deformed according to the tilt in the channel's walls. The assumed shape is shown on the right hand side of Fig. 14. The position of the bubble's centre is determined in addition to its diameter because the width of the channel is a function of the height z within the channel (compare Fig. 3). An estimate of the bubble's volume is given by using Eq. 1 with the channel's width $a(z)$ at the height of the bubble's centre.

The results are displayed in Figs. 15 and 16 for the groove and the wedge channels, respectively. The error bars represent the standard deviation of the averaged measurements. Both channels display similar behaviour when the flow rate is increased further than Q_{crit}. The
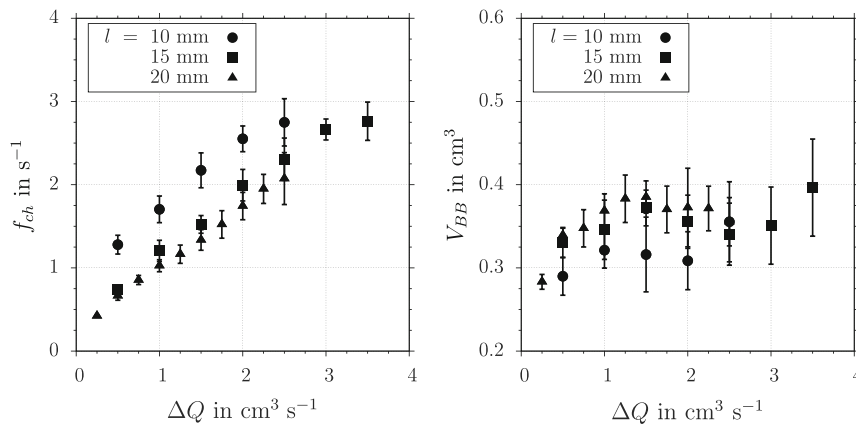

Fig. 15 Bubble ingestion frequency (*left*) and bubble volume (*right*) in the groove channel in EU1 at different supercritical flow rates with $\Delta Q = Q - Q_{crit}$. The error bars represent the standard deviation of the respective measurements
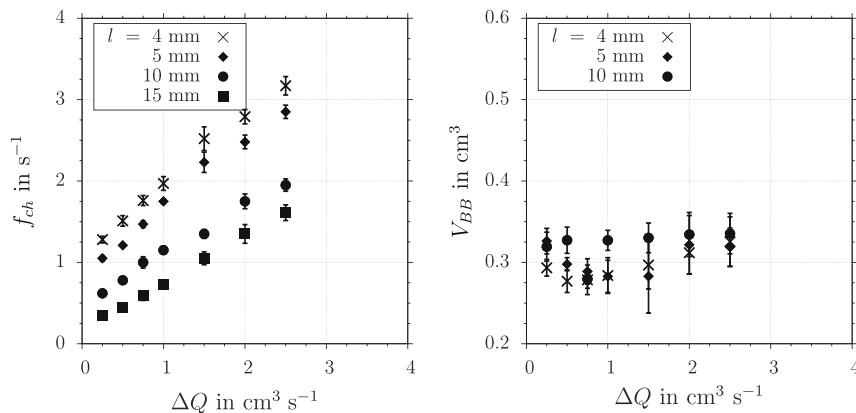

Fig. 16 Bubble ingestion frequency (*left*) and bubble volume (*right*) in the wedge channel in EU2 at different supercritical flow rates with $\Delta Q = Q - Q_{crit}$. The *error bars* represent the standard deviation of the respective measurements

ingestion frequency rises when the flow rate is increased. This dependency appears to be linear. Furthermore, it is observed that shorter channels produce higher frequencies than longer channels at identical ΔQ. The volume of the ingested bubbles appears to remain constant and displays no immediate dependency on the flow rate. Further work is required to understand the behaviour of the free surface and the gas ingestion process in supercritical flow and the trends that are shown here suggest that modelled predictions of V_{BB} and f_{ch} may be possible for other channel lengths and geometries.

4 Summary

The experiment set-up of open capillary channel flows in multiple channel geometries on board the ISS is presented. The experiments performed on the ISS included determining critical flow rates above which the free surface in the open capillary channel becomes unstable and gas is ingested into the flow. Critical flow rates for numerous channel lengths and for three different channel geometries are presented here.

Bubble volumes and ingestion frequencies are presented for various supercritical flow rates. The results suggest that the mean bubble volume is independent of the flow rate while the ingestion frequency displays a strong dependence on flow rate. The results of the transient, oscillatory, and two-phase flow experiments that were also performed on board the ISS will be published in the near future.

The experiment hardware is currently in storage on the ISS. Further experiments are planned and a reinstallation of the experiment hardware on board the ISS is expected to take place in summer 2013.

References

Brakke KA (1992) The surface evolver. Exp Math 1(2):141–165

Dreyer ME, Rosendahl U, Rath HJ (1998) Experimental investigation on flow rate limitations in open capillary flow. In: 34th AIAA/ASME/SAE/ASEE Joint Propulsion Conference, AIAA 98-3165

Grah A, Dreyer ME (2010) Dynamic stability analysis for capillary channel flow: one-dimensional and three-dimensional computations and the equivalent steady state technique. Phys Fluids 22(1):1–11

Grah A, Haake D, Rosendahl U, Klatte J, Dreyer ME (2008) Stability limits of unsteady open capillary channel flow. J Fluid Mech 600:271–289

Haake D, Klatte J, Grah A, Dreyer ME (2010) Flow rate limitation of steady convective dominated open capillary channel flows through a groove. Microgravity Sci Technol 22(2):129–138

Jaekle DE (1991) Propellant management device conceptual design and analysis: Vanes. In: 27th AIAA/SAE/ASME/ASEE Joint Propulsion Conference, AIAA 91-2172

Klatte J (2011) Capillary flow and collapse in wedge-shaped channels. PhD thesis, Universitaet Bremen

Klatte J, Haake D, Weislogel MM, Dreyer ME (2008) A fast numerical procedure for steady capillary flow in open channels. Acta Mech 201(1-4):269–276

Melin J, van der Wijngaart W, Stemme G (2005) Behaviour and design considerations for continuous flow closed-open-closed liquid microchannels. Lab Chip 5:682–686

Rosendahl U, Dreyer ME (2007) Design and performance of an experiment for the investigation of open capillary channel flows. Exp Fluids 42(5):683–696

Rosendahl U, Ohlhoff A, Dreyer ME, Rath HJ (2002) Investigation of forced liquid flows in open capillary channels. Microgravity Sci Technol 13(4):53–59

Rosendahl U, Ohlhoff A, Dreyer ME (2004) Choked flows in open capillary channels: theory, experiment and computations. J Fluid Mech 518:187–214

Rosendahl U, Grah A, Dreyer ME (2010) Convective dominated flows in open capillary channels. Phys Fluids 22(052102):1–13

Salim A, Colin C, Grah A, Dreyer ME (2010) Laminar bubbly flow in an open capillary channel in microgravity. Int J Multiph Flow 36(9):707–719

Spivey RA, Sheredy WA, Flores G (2008) An overview of the Microgravity Science Glovebox (MSG) facility, and the gravity-dependent phenomena research performed in the MSG on the International Space Station (ISS). In: 46th AIAA aerospace sciences meeting, AIAA-2008-0812

Weislogel MM, Thomas EA, Graf JC (2009) A novel device addressing design challenges for passive fluid phase separations aboard spacecraft. Microgravity Sci Technol 21(3):257–268

Zhao B, Moore JS, Beebe DJ (2001) Surface-directed liquid flow inside microchannels. Science 291(5506):1023–1026